Spaceborne transmitter - stationary receiver bistatic SAR Polarimetry - Experimental Results

Madalina Ciuca, Andrei Anghel, Remus Cacoveanu, Gabriel Vasile, Michel Gay, Silviu Ciochina

HAL Id: hal-03004391

https://hal.science/hal-03004391

Submitted on 13 Nov 2020

SPACEBORNE TRANSMITTER - STATIONARY RECEIVER BISTATIC SAR POLARIMETRY - EXPERIMENTAL RESULTS

Madalina Ciuca[*][§]   *Andrei Anghel*[§]   *Remus Cacoveanu*[§]
Gabriel Vasile[*]   *Michel Gay*[*]   *Silviu Ciochina*[§]

[*] Grenoble Image Parole Signal et Automatique (GIPSA-lab), Saint-Martin-d'Hères, France
[§] University POLITEHNICA of Bucharest, Bucharest, Romania

ABSTRACT

From simple scattering mechanism extraction and throughout more complex applications (e.g., land classification, disaster monitoring), polarimetry has become a key element for remote sensing. For the particular case of bistatic polarimetry, the development of a theoretical basis has not been yet aligned with a comprehensive experimental validation. At the moment, an exhaustive search across the polarimetric scientific literature will reveal that for true bistatic geometries (i.e., significant angular separation between transmitter and receiver), only a small number of qualitative investigations have been made and there is still work to be done. In the current paper, one of the most popular polarimetric decomposition methods ($H - \alpha$) is applied to dual-pol VV-VH data, in both bistatic (space-surface geometry with ground-based receiver) and monostatic configurations. Images from both geometries are displaying a common, urban scene. Comparing the obtained results, objective observations are presented.

Index Terms— bistatic geometry, bistatic polarimetry, dual-pol, entropy-alpha, ground-based receiver, Sentinel-1, Synthetic Aperture Radar (SAR), VV-VH.

1. INTRODUCTION

Polarimetry is a powerful technique for performing and enhancing remote sensing applications. However, from a geometrical point of view, the majority of existing investigations make use of data obtained by monostatic (collocated transmitter and receiver) acquisitions.

The interest towards exploiting the advantages offered by bistatic configurations has increased in the recent years: several bistatic airborne platforms have been used for experiments [1, 2, 3], preparing the way for future bistatic space-missions, of which a valuable precursor is the (quasi-) bistatic TerraSAR-X/Tandem-X satellite duo [4]. All this steps have questioned the current understanding for bistatic data analysis and have sparked the necessity of developing new (or adapting the existing) theoretical instruments and methods. A number of bistatic experiments, with polarimetric capabilities, and involving geometries with ground-based receivers and satellite [5] or airborne [6] transmitters, can be found in the literature. However, in these studies, the polarimetric interpretation is limited only to the display of the obtained set of images or their color composites. This paper presents the first experimental results of a polarimetric Entropy-Alpha (H-α) decomposition, performed on a set of synthetic aperture radar (SAR) dual-pol images, acquired in a space-surface configuration with transmitter of opportunity. Data from the equivalent Sentinel-1, monostatic, observation is available and the classification results of the two analyses are compared.

The paper is structured as follows: Section 2 is dedicated to a short review of the dual-pol H-α algorithm and Section 3 presents the most important results of the monostatic-bistatic polarimetric analysis. Lastly, the conclusions summarize the directions for further development.

2. DUAL-POLARISATION GENERAL THEORY

Due to trading costs, data rate, spatial resolution or coverage capabilities, new satellite missions have favored to adopt the use of only one single transmitting polarization and to employ polarimetric diversity at reception (linear polarization reception, V and H). Because of the increased availability in monostatic dual-polarimetric products, the last decade has shown a rising interest towards a better exploiting of the incomplete, dual-pol, signatures. Cloude has proposed in [7] a modification of the more general H-α algorithm for the case of dual-pol HH-HV and VV-VH modes. With small changes, the algorithm has also been applied for co-polar, HH-VV, acquisitions [8]. An extensive study regarding the H-α algorithm for the case of monostatic dual-polarimetry can be found in [9].

2.1. $H - \alpha$ **dual-pol algorithm**

There is no doubt that the H-α decomposition has evolved as a conventional method of analyzing dual-polarisation data. The general, quad-pol, algorithm is based on the eigen-decomposition of the coherency matrix, constructed using the Pauli basis vector. For dual-pol acquisitions, the computation will start from a different scattering vector: $\mathbf{k}_{dual} = [S_{xx} \; S_{xy}]^T$, and a 2x2 coherency matrix $\mathbf{J}$ will be constructed (the notation from [7] is preserved through the paper). In the following, xx stands for the co-polar VV or

HH, and *xy* for the cross-polar VH or HV (alternatively, both co-polar HH and VV can be taken into consideration). $< \cdot >$ signifies an averaging operation.

$$\mathbf{J} = \left\langle \mathbf{k}_{dual} \cdot \mathbf{k}_{dual}^H \right\rangle$$

$$= \begin{bmatrix} \langle S_{xx} S_{xx}^* \rangle & \langle S_{xx} S_{xy}^* \rangle \\ \langle S_{xy} S_{xx}^* \rangle & \langle S_{xy} S_{xy}^* \rangle \end{bmatrix} = \sum_{i=1}^{2} \lambda_i \mathbf{u}_i \mathbf{u}_i^H \quad (1)$$

with $\lambda_1 \geq \lambda_2$ and $\mathbf{u}_i = [\cos(\alpha_i) \sin(\alpha_i) \cos(\beta_i) e^{j\delta_i}]^T$

The entropy (H) and alpha (α) parameters are obtained from the eigenvalues (λ_i) and by a weighted average of the α_i angles (extracted from each eigenvector, $\mathbf{u}_i$). Using the orthogonality property, its expression can be simplified as in eq. (4). The values of β_i and δ_i are not of interest for the current analysis.

$$p_i = \frac{\lambda_i}{\sum_{i=1}^{2} \lambda_i} \quad (2)$$

$$H = -\sum_{i=1}^{2} p_i \log_2(p_i) \quad (3)$$

$$\alpha = p_1 * \arccos\left(\mathbf{u}_1(1)\right) + p_2 * \left[\frac{\pi}{2} - \arccos\left(\mathbf{u}_1(1)\right)\right] \quad (4)$$

In the original definition, both H and α are invariant descriptors of the scattering mechanism. However, in the case of dual-pol measurements, the α angle is no longer invariant and its interpretation, which depends on the specific dual-pol mode (e.g., HH-VV, VV-HV, hybrid), may not be yet fully understood [9, 10, 11].

2.2. Amplitude and phase channel imbalances

For extracting the correct scattering matrices, calibration and compensation operations must be performed to the polarimetric measurements, with the primary goal to eliminate the effect of distortions (at transmission, reception and over the propagation path) [12]. In the following, we are interested in evaluating the influence of uncalibrated phase and amplitude components in a dual-pol measurement, and their propagation and influence over the dual-pol 2x2 coherency matrix. A superscript "*u*" is added to those elements that are considered uncalibrated. As a result, we can write:

$$\begin{bmatrix} S_{xx}^u \\ S_{xy}^u \end{bmatrix} = \begin{bmatrix} S_{xx} \\ a \cdot e^{-j\delta_r} S_{xy} \end{bmatrix} \quad (5)$$

where $\delta_r = \frac{2\pi}{\lambda} \Delta r$ models a relative phase imbalance between the *xy-xx* receiving channels, while a quantifies for an amplitude imbalance. When computing the eigenvalues of the 2x2 coherency matrix, **J**, we observe that the phase imbalance will have no relevant influence, while the uncalibrated amplitude errors are not to be ignored, as shown in eq. 7.

$$\begin{vmatrix} J_{1,1}^u - \lambda & J_{1,2}^u \\ J_{1,2}^{u*} & J_{2,2}^u - \lambda \end{vmatrix} = 0 \quad (6)$$

$$\Leftrightarrow (J_{1,1} - \lambda)(a^2 \cdot J_{2,2} - \lambda) - a^2 \cdot |J_{1,2}|^2 = 0 \quad (7)$$

It can be shown analytically that the phase imbalance has an impact only on the δ_i component of the eigenvector, which does not influence the entropy and α parameters.

As a result, phase imbalances should have little effect over the final entropy and α values, while important alterations can appear in the presence of amplitude errors.
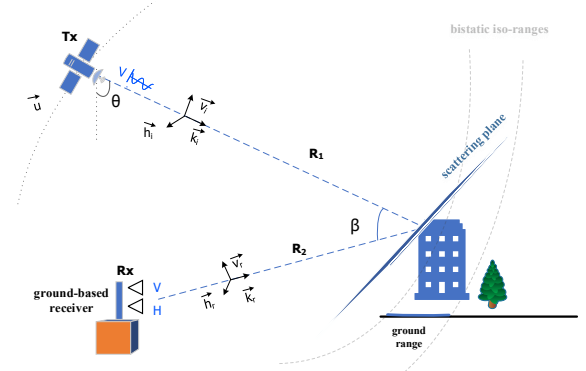
3. EXPERIMENTAL RESULTS

Fig. 1: General bistatic space - surface acquisition geometry.

A set of bistatic images in dual-polarisation were acquired in a single-pass in autumn 2019, by the ground-based receiver described in [13]. Two antennas with orthogonal polarisations were used for sensing the H and V components of the scattered electric field, from an area of Bucharest city, Romania. The Sentinel-1A/B is used as transmitter of opportunity. For the specific latitude, the satellite operates in the Interferometric Wide (IW) Swath mode and transmits radio pulses in linear, vertical polarisation (V). Fig. 1 shows a schematic representation of the bistatic geometry. The bistatic angle (β), for this particular geometry, is around $56°$. The propagation unit vectors, $\vec{k_i}, \vec{k_r}$ are represented in the BSA (Back Scatter Alignment) convention.

The inspected zone contains different type of reflectors, as it integrates an urban area, construction sites, semi-urban terrains covered with vegetation, an artificial lake and a dam. The bistatic SAR data, alongside their correspondent monostatic acquisitions from Sentinel-1, were focused on the same grid, which is aligned with the local latitude and longitude and has a 2 x 2 m pixel spacing. The position of the receiver is taken as origin of the local latitude/longitude axes. Because the difference in altitude between the receiver (GPS value of 165 m) and the observed scene is only in the order of several dozens of meters, the bistatic scene appears very sparse compared to the monostatic one. A dual-polarisation composite monostatic RGB image is illustrated in Fig. 2a. Side by side, the bistatic composite image can be seen in Fig. 2b (only the set of pixels exceeding a given threshold value are used). A general comparison can rapidly discover that the bistatic image offers access to complementary information about the scene. For example, near the dam margin and
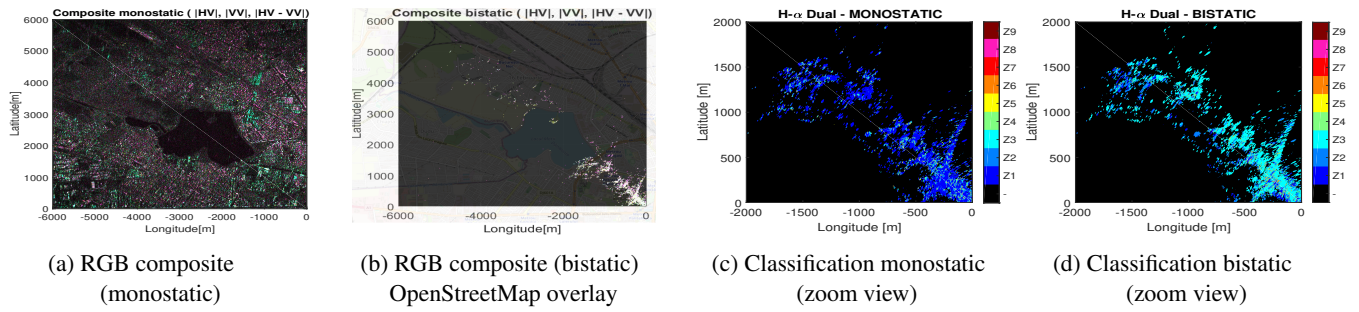
(a) RGB composite (monostatic)

(b) RGB composite (bistatic) OpenStreetMap overlay

(c) Classification monostatic (zoom view)

(d) Classification bistatic (zoom view)

Fig. 2: Selection of polarimetric results.

the lake's peninsula, a group of points of high reflectivity, not contained in the monostatic image, can be observed.

As part of a vertical, fixed, linear array, the two antennas used for the acquisition have been located at different heights (almost 1 m separation). Due to this constrained geometry, an additional phase imbalance is introduced between acquisitions. Besides it, other major possible sources of error are considered compensated or negligible. Precise synchronization between transmitter and receiver diminishes phase errors, while good channel isolation is considered to significantly reduce cross-talk at reception. A possible amplitude imbalance between the two bistatic receiving channels should not exceed fractions of dB for the bistatic acquisition and should not have a major impact. As a result and based on the observations from the previous section, the computation of the H and α parameters should remain valid, even considering the eventual phase imbalance resulting from geometry.

In dual-pol, the two curves delimiting the feasible and unfeasible zones of the $H - \alpha$ plane are symmetric with respect to the α parameter (45° axis of symmetry), for both monostatic and bistatic acquisitions. As in quad-pol, there are 8 feasible and 1 unfeasible zones. In [9], the average limits for an optimal delimitation of the different zones have been defined (for monostatic, VV-VH, dual-pol). These limits will be considered in the following analysis (for both monostatic and bistatic, dual-pol).

It has been identified that generally, in both monostatic and bistatic classifications, the entropy appears concentrated towards smaller values (quasi-deterministic mechanism). This observation is expected to be generally true for the parts of the scene representing dominant urban environments. Neither the monostatic, nor the bistatic, VV-VH dual-pol modes is capable of classifying scatterers with high entropy. This observation has been already mentioned in the literature, for the case of monostatic acquisitions, as a result of the lack of information from the other co-polar mechanism.

When comparing simple monostatic and bistatic $H - \alpha$ classification maps, differences and zone translations can be observed. A valid example can be seen in Figs. 2c and 2d, which offer a truncated, magnified view, from the lower right corner of the original classifications. The transitions are primarily between areas of small entropy, where the α mechanism appears to suffer some changes: it presents small and

medium values in the monostatic case and medium and high values in the bistatic one. Only the set of common pixels extracted from both the bistatic and monostatic images by a common filtering mask (a thresholding value for the amplitude of the pixels in the bistatic image) have been considered as a starting point for performing the classifications.

Fig. 3 displays the depiction in the dual-pol H-α plane of the set of scatterers which do not present any zone translation between their monostatic and bistatic representations (they are figuratively named "persistent" scatterers). These pixels correspond to the elements from the diagonal of Table 1, in which the general statistics of the scattering mechanism translations (from monostatic to bistatic, over the set of common points) are displayed in percentage.

A critical migration of points appears near small entropies. It can be easily identified a general pixel movement towards zones of dipole and dihedral reflection mechanisms, near small entropies. For example, approximately 35% of the pixels from Z1 appear to have migrated to Z3, in the bistatic classification. Furthermore, it can be seen that there is a general tendency of translations towards Z3 (bistatic) from all zones of the (monostatic) plane.
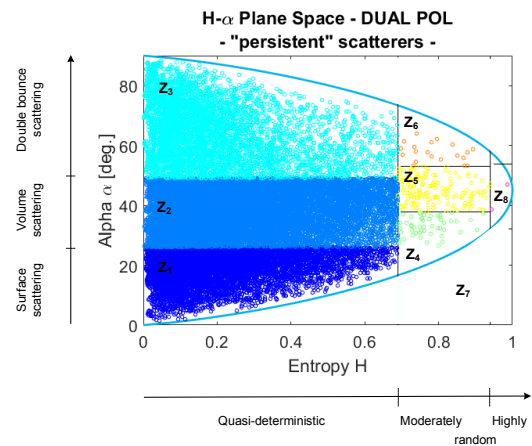

Fig. 3: H-α Plane - Distribution of pixels having the same scattering mechanism in both monostatic and bistatic dual-pol.

Table 1: Scattering mechanism retention ratio from monostatic to bistatic.

Monostatic classif.[%]	Bistatic classif. [%]							
	Z1	Z2	Z3	Z4	Z5	Z6	Z8	Z9
Z1	**4.72**	**18.56**	**35.26**	0.38	1.26	0.54	0.007	0.002
Z2	**2.19**	**8.40**	**15.56**	0.15	0.45	0.21	0.002	4e−4
Z3	0.37	**1.18**	**2.41**	0.02	0.06	0.04	0.005	0
Z4	0.26	0.99	1.77	**0.02**	0.06	0.02	0.005	0
Z5	0.32	1.02	2.12	0.02	**0.07**	0.04	4.3e−4	0
Z6	0.07	0.24	0.52	0.002	0.02	**0.009**	0.002	0
Z8	0.05	0.15	0.31	0.003	0.01	0.004	**0.001**	0
Z9	4e−4	0.002	0.003	0	4e−4	0	0	**0**

Legend H-α zones

- Z9 - Complex structures
- Z8 - Random anisotropic
- Z7 - Unfeasible zone
- Z6 - Multiple double reflections
- Z5 - Anisotropic particles
- Z4 - Random surface
- Z3 - Dihedral reflector
- Z2 - Dipole feature
- Z1 - Bragg surface

4. CONCLUSIONS

After comparing the two classification results, some general conclusions can be extracted. Firstly, in both monostatic and bistatic, the use of partial polarimetric diversity, dual-pol VV-VH, appears to impact in a similar way the discrimination possibility of the entropy mechanism (lack of co-polar information). Secondly, it is clear that the change of the α parameter from monostatic to bistatic, should be further investigated. It is important to examine if the optimal limits for the $H - \alpha$ zones discrimination have changed in the bistatic case and, if so, study the new correspondence for the values of the parameters (with an emphasis on the average scattering angle, α). For some particular zones, compared to the results from [9], the general diffusion mechanism from monostatic to bistatic (dual-pol, VV-VH), has the opposite direction of migration from the one shown to appear at the change from full-polarisation to VV-VH dual-pol (monostatic).

For an improved analysis, a reiteration of the bistatic polarimetric acquisition will be performed for the case when both phase centers of the receiving elements are at the exact same location. For increased classification accuracy, the amplitude imbalance between acquisitions should be more precisely evaluated.

5. REFERENCES

[1] A. Meta *et al.*, "First Results of the BelSAR L Band Airborne Bistatic Fully Polarimetric Synthetic Aperture Radar Campaign," in *Proc. of IGARSS*, Jul. 2017, pp. 1040–1042.

[2] A.S. Goh *et al.*, "Bistatic SAR Experiment with the Ingara Imaging Radar," *IET Radar Sonar Navig.*, vol. 4, no. 3, pp. 426–437, Sept. 2010.

[3] P. Dubois *et all*, "ONERA-DLR Bistatic SAR Campaign: Planning, Data acquisition and First Analysis of bistatic scattering Behaviour of Natural and Urban Targets," in *IEEE Proc. Radar Sonar Navig.*, Jun. 2006, vol. 153, pp. 215–223.

[4] J. Bueso-Bello *et al.*, "Performance Evaluation of TanDEM-X Quad-Polarization Products in Bistatic Mode," *IEEE J. Sel. Topics Appl. Earth Observ. Remote Sens.*, vol. 11, no. 3, pp. 787–799, Mar. 2018.

[5] H. Nies *et al.*, "Polarimetric and Interferometric Applications in a Bistatic Hybrid SAR Mode using TerraSAR-X," in *Proc. of IGARSS*, Jul. 2010, pp. 110–113.

[6] A. Barmettler *et al.*, "Swiss Airborne Monostatic and Bistatic Dual-Pol SAR Experiment at the VHF-Band," in *Proc. of EUSAR*, Jun. 2008, pp. 1–4.

[7] S. Cloude, "The Dual Polarisation Entropy/Alpha Decomposition: A PALSAR Case Study," in *Proc. of PolInSAR*, Mar. 2007, pp. 1–6.

[8] L. Xie *et al.*, "Similarity Analysis of Entropy/Alpha Decomposition between HH/VV Dual and Quad-polarization SAR data," *IEEE Geosci. Remote Sens. Lett.*, vol. 6, no. 3, pp. 228–237, Mar. 2015.

[9] K. Ji *et al.*, "Scattering Mechanism Extraction by a Modified Cloude-Pottier Decomposition for Dual Polarization SAR," *Int. Journal of Remote Sensing*, vol. 7, no. 6, pp. 7447–7470, Jun. 2015.

[10] T. Ainsworth *et al.*, "Classification Comparisons Between Dual-pol and Quad-pol SAR Imagery," in *Proc. of IGARSS*, Jul. 2007, pp. 164–167.

[11] S. Azadnejada c*et al.*, "Evaluation of Polarimetric Capabilities of Dual Polarized Sentinel-1 and TerraSAR-X Data to Improve the PSInSAR Algorithm using Amplitude Dispersion Index Optimization," *Int. J Appl. Earth Obs. Geoinformation*, vol. 84, pp. 1–11, Febr. 2020.

[12] M. Shimada *et al.*, "PALSAR Radiometric and Geometric Calibration," *IEEE Trans. Geosci. Remote Sens.*, vol. 47, no. 12, pp. 3915–3932, Dec. 2009.

[13] A. Anghel *et al.*, "COBIS: Opportunistic C-Band Bistatic SAR Differential Interferometry," *IEEE J. Sel. Topics Appl. Earth Observ. Remote Sens.*, vol. 12, no. 10, pp. 3980–3998, Oct. 2019.